



Near-infrared responsive Z-scheme heterojunction with strong stability and ultra-high quantum efficiency constructed by lanthanide-doped glass

Guobiao Li^a, Shouqiang Huang^b, Ke Li^a, Nanwen Zhu^{c,d,*}, Bofeng Zhao^a, Qi Zhong^a, Zhihan Zhang^a, Dongdong Ge^b, Dong Wang^{a,e,**}

^a Ganjiang Innovation Academy, Chinese Academy of Sciences, Ganzhou 341000, PR China

^b Jiangsu Key Laboratory of E-waste Recycling, School of Chemistry and Environmental Engineering, Jiangsu University of Technology, Changzhou 213001, PR China

^c Shanghai Engineering Research Center of Solid Waste Treatment and Resource Recovery, School of Environmental Science and Engineering, Shanghai Jiao Tong University, Shanghai 200240, PR China

^d Shanghai Institute of Pollution Control and Ecological Security, Shanghai 200092, PR China

^e Key Laboratory of Green Process and Engineering, National Engineering Research Center of Green Recycling for Strategic Metal Resources, Institute of Process Engineering, Chinese Academy of Sciences, Beijing 100190, PR China

ARTICLE INFO

Keywords:

NIR photocatalyst
Z-scheme heterojunction
Upconversion glass-ceramic
Stability
Built-in electric field

ABSTRACT

Lanthanide-doped near-infrared (NIR) photocatalyst still obstructed by the less impressive photocatalytic efficiency and stability. In this work, we report a novel strategy by introducing the lanthanide-doped ferroelectric perovskites of SrTiO_3 and $\text{Sr}_2\text{Bi}_4\text{Ti}_4\text{O}_{15}$ into the glass-ceramic (GC), then an efficient and stable NIR photocatalyst was fabricated through the method of facile in-situ HCl etching GC. The results show that $\text{Sr}_2\text{Bi}_4\text{Ti}_4\text{O}_{15}$, SrTiO_3 , and BiOCl were exposed to the superficial coating of the core-shell structured photocatalyst and constructed Z-scheme heterojunction, the heterojunction with built-in electric field could significantly facilitate the charge carriers separation and harvest NIR light for photocatalytic reaction simultaneously. The evident increase of Lewis basic sites over defect-rich photocatalyst is found, the $\cdot\text{O}_2^-$ and $\cdot\text{OH}$ radicals are generated. During the degradation of norfloxacin (NOR) under NIR light irradiation for 90 min, the NOR degradation rate is 86% (TOC removal rate is 30.7%), the high apparent quantum yield of 2.3% is achieved.

1. Introduction

In recent years, antibiotics were extensively used as drugs to treat human and animal which led to more and more environmental pollution and threats to the balance of the ecosystem and human health [1]. Photocatalytic technology has provided a promising approach to solve the problems in the fields of organic pollution removal [2,3]. However, most of these semiconductor photocatalysts require high energy photon (ultraviolet and visible light) activation, the intrinsic challenges such as the low light penetration and energy ratio, light competition between pollutant and photocatalyst, which lead to the limited photocatalytic efficiency and inhibit the wide application of photocatalysis [2]. Typically, a widely used antibiotic of norfloxacin (NOR) enters deep waters (e.g., rivers or lakes) that UV and visible light are difficult to reach. Compared with ultraviolet light, near-infrared (NIR) light responsive

photocatalyst has been proved that can overcome the challenges by utilizing the high penetration and energy ratio of NIR light, which can be provided with an ideal penetration depth through various media, notably biological tissue and wastewater [2–5].

The lanthanide-doped NIR photocatalyst is the most widely available, the energy transfer mechanisms can be directly absorption (DA), emission-reabsorption (ER), and Förster resonance energy transfer (FRET) [6]. The NIR photocatalyst can be divided into two types which are lanthanide direct doping and core-shell structure. Directly dope lanthanide ions into semiconductor can increase the light energy utilization and promote the separation efficiency of e^-h^+ , simultaneously [7], however, the upconversion luminescence efficiency of the type of NIR photocatalyst is not high enough, which limits the NIR photocatalytic activity [8]. The core-shell structure type of NIR photocatalyst is combined with the luminescent matrix and semiconductor, where the

* Corresponding author at: Shanghai Engineering Research Center of Solid Waste Treatment and Resource Recovery, School of Environmental Science and Engineering, Shanghai Jiao Tong University, Shanghai 200240, PR China.

** Corresponding author at: Ganjiang Innovation Academy, Chinese Academy of Sciences, Ganzhou 341000, PR China.

E-mail addresses: nwzhu@sjtu.edu.cn (N. Zhu), wangdong@ipe.ac.cn (D. Wang).

<https://doi.org/10.1016/j.apcatb.2022.121363>

Received 10 January 2022; Received in revised form 12 March 2022; Accepted 28 March 2022

Available online 6 April 2022

0926-3373/© 2022 Elsevier B.V. All rights reserved.

lanthanide ion doped optically active centers are displayed as the cores, and the semiconductor is as the superficial coating. The NIR photocatalyst of $\text{NaYF}_4: \text{Yb}^{3+}, \text{Gd}^{3+}, \text{Tm}^{3+} @ \text{Bi}_2\text{WO}_6$ [9], $\text{NaYF}_4: \text{Yb}^{3+}, \text{Nd}^{3+} @ \text{TiO}_2$ [10] can harvest the NIR photons and emit upconversion luminescence, which is can utilized by themselves for photocatalysis under NIR light irradiation. It should be noted that water molecules, metal ions, and organic compound in directly contact with optically active centers can quench upconversion luminescence [11]. Naturally, the unstable combination interface between luminescent matrix and semiconductor may affect luminous efficiency, and the interfacial defects could act as quenchers or recombination centers of e^-h^+ , which can limit the photocatalytic activity under NIR irradiation [12]. In addition, the two types of NIR photocatalysts have low photocatalytic efficiency under NIR irradiation, the drawback of the tedious preparation process and the large scale preparation is arduous [6,13], therefore, an innovative strategy of constructing stable and efficient NIR photocatalyst should be explored.

The glass-ceramics (GC) have attracted research interest for excellent environmental applications, high and stable upconversion efficiency, owing to the facile fabrication process, regenerative, the flexibility of shape, and suitable for large-scale production [3,6,13–15]. In our previous studies, we first developed a regenerative and efficient NIR GC photocatalyst through the method of HBr and HCl (or Cl^- contained concentrated leachate) etching upconversion GC (FIEG) [3,6,13], where the BiOBr and BiOCl nanosheet was in-situ grown on the surface of the NIR GC photocatalysts to improve expose active sites, and GC with the lanthanide-doped upconversion luminescence matrix (SrF_2) as the core, the efficient and stable photocatalytic performance under NIR irradiation were presented [3,6]. However, the exposure of SrF_2 on the superficial coat can affect the photocatalytic active sites, furthermore, it cannot help to improve the charge carrier separation, because there is no feature of semiconductor of SrF_2 to construct heterojunction with the surface photocatalyst. Therefore, choosing a semiconductor that can achieve upconversion luminescence can not only emit light, but also construct heterojunction. Fortunately, the impediment can be resolved by introducing semiconductors that can upconvert luminescence.

It has been demonstrated that perovskite oxides usually manifest better charge carrier separation due to their higher lattice distortion as compared to the traditional binary oxides [16,17]. Typically, the spontaneous polarization generated from the ferroelectric SrTiO_3 immensely improves the charge separation efficiency of semiconductor photocatalyst, thus giving rise to high photocatalytic performance [18]. Recent studies have shown that the overall water splitting at an external quantum efficiency of up to 96% could be obtained by using a modified Al-doped SrTiO_3 photocatalyst [19]. Meanwhile, $\text{SrBi}_4\text{Ti}_4\text{O}_{15}$ is located at the intersection of traditional ferroelectric, layered bismuth-based semiconductor, and perovskite-structured crystal, which has been proved to be powerfully applied for photocatalysis [16]. In addition, rare-earth ions doped SrTiO_3 [20] and $\text{SrBi}_4\text{Ti}_4\text{O}_{15}$ [21] enable to apply for the upconversion based applications. Therefore, it can gather all the above benefits of SrTiO_3 and $\text{SrBi}_4\text{Ti}_4\text{O}_{15}$ to demonstrate powerfully applied for photocatalysis and upconversion in the NIR GC photocatalyst.

In the present investigation, we try to introduce the rare-earth ions ($\text{Yb}^{3+}/\text{Er}^{3+}$) doped upconversion luminescent matrix of SrTiO_3 and $\text{SrBi}_4\text{Ti}_4\text{O}_{15}$ into the $\text{Bi}_2\text{O}_3\text{-B}_2\text{O}_3$ glass, afterwards, the novel photocatalyst with the coat of BiOCl nanosheets growing on surfaces of the $\text{SrCO}_3\text{-Bi}_2\text{O}_3\text{-B}_2\text{O}_3\text{-TiO}_2$ (SBBT) GC micro-particle was synthesized via FIEG. The photocatalyst absorb NIR light and upconvert shortwave for photocatalytic degradation, the heterojunction of $\text{SrTiO}_3/\text{SrBi}_4\text{Ti}_4\text{O}_{15} @ \text{BiOCl}$ in GC can be constructed during the FIEG, which largely improve the separation of e^-h^+ and photocatalytic activities. The density of states and difference charge density were calculated by density functional theory (DFT), to reveal the charge transfer mechanism of the heterojunction. The degradation pathways of NOR during the photocatalysis and the photodegradation of low concentration antibiotics

contained real wastewater with was studied. In addition, the regeneration behavior of photocatalytic activity and feasibility of large-scale synthesis are analyzed.

2. Experimental

2.1. Reagents

Reagents of SrCO_3 , Bi_2O_3 , TiO_2 , B_2O_3 , Er_2O_3 , Yb_2O_3 , HCl , and BiOCl (99.8%) were analytical purity purchased from Sinopharm Chemical Reagent Co. Ltd in China. The formic acid, acetonitrile, and the methanol was chromatographic purity obtained from Shanghai Anpu CNW. The raw concentrated leachate (CL) water quality parameters: $\text{pH} = 7.2$, Total nitrogen (TN) = 158.2 mg/L, the total organic carbon (TOC) = 2087.1 mg/L, acquired from the municipal solidwaste landfill (Changzhou, China) and filtered to remove particles impurities.

2.2. Synthesis of upconversion GC

The content (mol%) of GC $\text{SrCO}_3\text{-Bi}_2\text{O}_3\text{-B}_2\text{O}_3\text{-TiO}_2$ (SBBT) are: 30% $\text{Bi}_2\text{O}_3\text{-21}\%\text{TiO}_2\text{-21}\%\text{SrCO}_3\text{-21}\%\text{B}_2\text{O}_3\text{-5}\%\text{Yb}_2\text{O}_3\text{-2}\%\text{Er}_2\text{O}_3$. The SBBT parent glass was fabricated as described in the literature [22]. The SBBT-UPG samples were reheat at 350, 400, 450, 500, 550, and 600 °C with 5 °C/min and crystallized 60 min for obtaining targeted GC, the micron-scaled SBBT-GC particle was achieved by milling for 10 min, which was SBBT-GC350, SBBT-GC400, SBBT-GC450, SBBT-GC500, SBBT-GC550, and SBBT-GC600.

2.3. Synthesis of NIR heterojunction

The SBBT-GC samples were stirred in 0.05, 0.1, and 0.2 mol/L HCl solution for 15 min with a stirring rate of 500 r/min, the heterojunction was acquired after distilled water washed and dried, which were labeled as SBBT-SS@B-0.05HCl, SBBT-SS@B-0.1HCl, and SBBT-SS@B-0.2HCl (Fig. 1).

2.4. Analysis

The phase of heterojunction detected by Bruker D8 of X-ray diffraction (XRD). Microstructure was analyzed by the Sirion 200 the scanning electron microscope (SEM), the transmission electron microscope (TEM) was tested via TALOS F200X. XPS was detected through Kratos Axis Ultra DLD which calibrated by the 284.8 eV (C1s). The absorption spectra were tested by the Lambda 950 UV-vis-NIR spectrophotometer. Upconversion spectra and photoluminescence spectra (PL) was calibrated by the fluorescence spectrophotometer (Hitachi F-7000). Photoelectro-chemical performance of sample was via the CHI 760E electrochemical workstation. The Brunauer-Emmett-Teller (BET) of photocatalysts were analyzed through Quantachrome Autosorb-IQ. Decay curves were tested by the FluoroMax Plus equipped with a 980 nm pulsed laser. CO_2 and NH_3 adsorption on the BiOCl and SBBT-

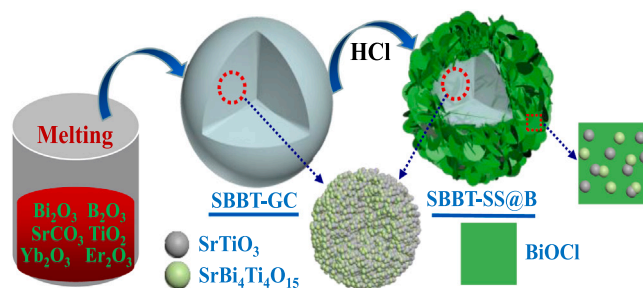


Fig. 1. Schematic for the synthesis of the perovskite heterojunction photocatalyst via the FIEG.

SS@B-0.1HCl were tested by temperature-programmed desorption (TPD) using a chemisorption Analyzer (AutoChem II 2920, Micromeritics). Electron spin resonance (ESR) spectral analysis was performed on Bruker A300 spectrometer to find out the free radical generation and oxygen vacancy during photocatalytic processing. The NOR photodegradation intermediates and concentration was analyzed via the UPLC-SQD2 (the antibiotics test conditions show in [Supplementary Material](#), [Table S1](#), and [Table S2](#)).

2.5. Photocatalytic experiment

The photocatalytic activities of the heterojunction were performed on the degradation of NOR (20 mg/L, 20 mL) under NIR irradiation (1000 W mercury lamp, $\lambda \geq 780$ nm) and UV-vis-NIR light (500 W xenon lamp), 20 mg photocatalyst was added to the NOR wastewater ([Fig. S1](#)).

2.6. Regenerate the material for recyclability test

After 3 cycles, the SBBT-SS@B-0.1HCl were further stirred with 500 r/min at excess HCl (0.1 mol/L) for another 90 s. Then, the regenerated SBBT-SS@B-0.1HCl was acquired after washed and drying.

2.7. Methods of DFT calculations

The present first principle DFT calculations are performed by Vienna Ab initio Simulation Package (VASP) [23] with the projector augmented wave (PAW) method [24]. The exchange-functional is treated using the Perdew-Burke-Ernzerhof (PBE) functional [25], in combination with the DFT-D correction [26]. The cut-off energy of the plane-wave basis is set at 500 eV for the optimization of both geometry and lattice size. The Brillouin zone integration is performed with a $3 \times 3 \times 1$ Gamma k-point sampling for the $\text{Sr}_{0.93}\text{TiYb}_{0.05}\text{Er}_{0.02}\text{O}_3$ (110) / BiOCl (110) heterojunction structure. The self-consistent calculations apply a convergence energy threshold of 10^{-5} eV. The equilibrium geometries and lattice

constants are optimized with maximum stress on each atom within 0.02 eV/Å.

3. Result and discussion

3.1. Perovskite GC

XRD of SBBT-UPG and SBBT-GC as shown in [Fig. 2a](#), only the diffuse hump-peak emerged in SBBT-UPG, which indicates the noncrystalline structure in SBBT-UPG. The crystallization temperature is vital to improve the crystallinity [27,28], and to optimize crystallization temperature for perovskites crystallizing in SBBT-GC, five crystallization temperatures were performed. All of the diffraction peaks of the SBBT-GC samples are determined as the perovskite of SrTiO_3 and $\text{Sr}_2\text{Bi}_4\text{Ti}_4\text{O}_{15}$. Meanwhile, it could discover that the crystallization temperatures are related to the crystallinity of perovskites of SrTiO_3 and $\text{Sr}_2\text{Bi}_4\text{Ti}_4\text{O}_{15}$, since the temperatures directly affect their contents and crystal sizes. Between 350 and 500 °C, the increase of crystallization temperature contributed to optimal nucleation and crystallization of SrTiO_3 . After the optimum crystallization temperature of 500 °C, the excessive temperature, such as 550 °C, will lead to the destruction of SrTiO_3 crystals, a similar result is also found in the $\text{Sr}_2\text{Bi}_4\text{Ti}_4\text{O}_{15}$ crystals.

The upconversion emission spectra are shown in [Fig. 2b](#), the blue (485 nm), green (527, 545, and 551 nm), and red (657 nm) emission is obtained, which are identified as $^4\text{F}_{7/2} \rightarrow ^4\text{I}_{15/2}$, $^2\text{H}_{11/2} \rightarrow ^4\text{I}_{15/2}$, $^4\text{S}_{3/2} \rightarrow ^4\text{I}_{15/2}$, $^4\text{S}_{3/2} \rightarrow ^4\text{I}_{15/2}$, and $^4\text{F}_{9/2} \rightarrow ^4\text{I}_{15/2}$ transitions of Er^{3+} ions, respectively [20]. The tendency of the upconversion emission intensities are similar to that of the XRD diffraction peaks intensities of SrTiO_3 , and both of them achieve the optimum over the SBBT-GC500 sample. The SBBT-GC500 presents strong upconversion luminescence owing to the increasing crystallinity of $\text{Er}^{3+}/\text{Yb}^{3+}$ doped luminescent matrix (perovskites of SrTiO_3 and $\text{Sr}_2\text{Bi}_4\text{Ti}_4\text{O}_{15}$), for the perovskites provide the low phonon energy to promote upconversion emission efficiency and SrTiO_3 with the lower phonon energy than that of $\text{Sr}_2\text{Bi}_4\text{Ti}_4\text{O}_{15}$ [20,28]. According to the degradation rates results of NOR under NIR

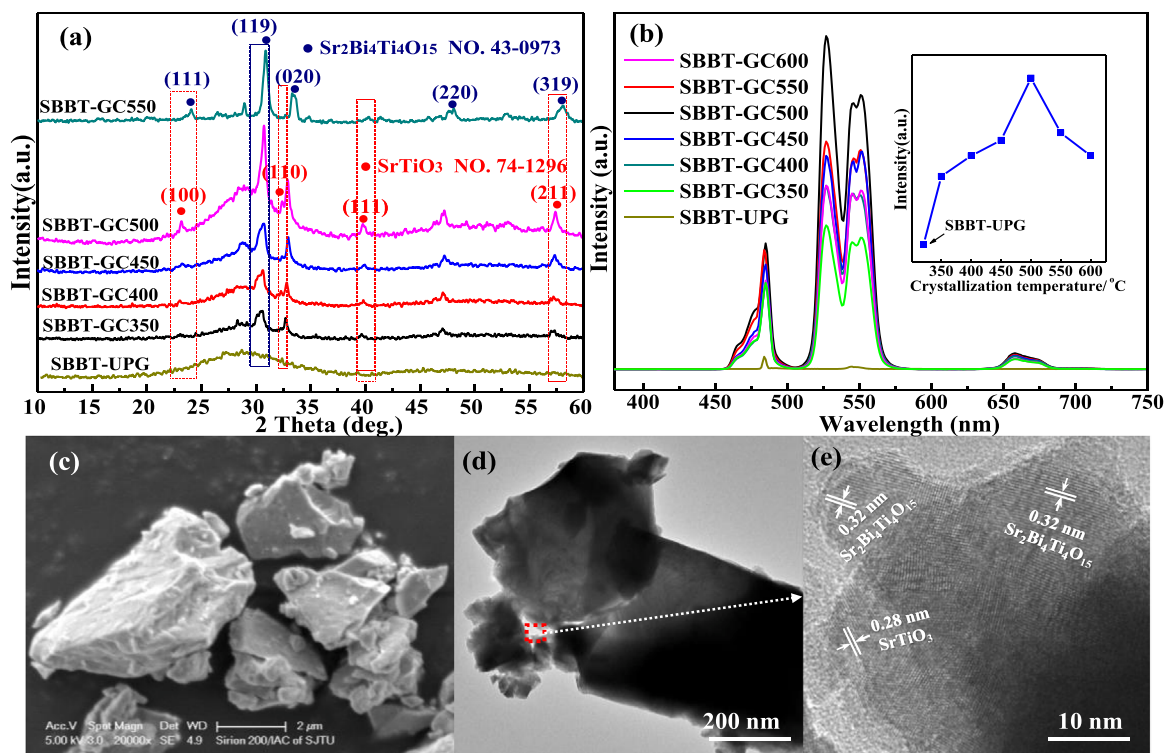


Fig. 2. (a) XRD and (b) upconversion luminescence spectra (under 980 nm NIR excitation, current = 2 A) of SBBT-UPG and SBBT-GC. (c) SEM, (d) TEM, and (e) HRTEM images of SBBT-GC500.

($\lambda \geq 780$ nm) irradiation with different crystallization temperatures (Fig. S2a) and etching times (Fig. S2b), SBBT-GC500 is chosen as the etching samples, and the best etching time is 15 min

The SEM/TEM images of SBBT-GC500 as shown in Fig. 2c and d, and the irregular particles of 0.1–5 μm are presented. The TEM and HRTEM images and the enlarged appearances are shown in Fig. S3, which abundant dots (< 10 nm) are presented in GC microparticles. A corresponding HRTEM image (Fig. 2e) includes lattice fringe of 0.32 nm that is belong to the (109) planes of $\text{Sr}_2\text{Bi}_4\text{Ti}_4\text{O}_{15}$, and the lattice of 0.28 nm is attributed to the (110) plane of the SrTiO_3 phase.

3.2. NIR GC photocatalysts characterization

To in-situ grown BiOCl on SBBT-GC500 through FIEG to fabricate NIR GC photocatalysts, SBBT-GC500 was etched in 0.05, 0.1, and 0.2 mol/L HCl for 15 min, XRD results are shown in Fig. 3a. The BiOCl phase appears in SBBT-SS@B-0.05HCl, SBBT-SS@B-0.1HCl, and SBBT-SS@B-0.2HCl. The crystallization peaks of BiOCl increase gradually as the increasing of HCl concentration from 0.05 to 0.2 mol/L, and those of SrTiO_3 and $\text{Sr}_2\text{Bi}_4\text{Ti}_4\text{O}_{15}$ in GC gradually weaken and disappeared. The diffraction peak of BiOCl in photocatalyst is reduced and red-shifted compared with that of typical pure BiOCl (Fig. S4), which owing to quiet a few ions doping into BiOCl during the etching process [29]. The diffraction peaks of SrTiO_3 and $\text{Sr}_2\text{Bi}_4\text{Ti}_4\text{O}_{15}$ remain in the photocatalysts which contribute to the construction of heterojunction.

Fig. 3b shows the SEM images of SBBT-SS@B-0.1HCl, and it can be observed that the surface of SBBT-SS@B-0.1HCl is coated by abundant nanosheet (about 500 nm). Especially, nanosheet is vertically aligned shown in Fig. 3c, which contribute to producing abundant pores and increasing reactive sites exposed during the photocatalysis, and the root of the nanosheets are implanted in a superficial coat of GC.

Fig. 3d shows the N_2 adsorption-desorption isotherms and the

corresponding pore size distribution curves of the SBBT-SS@B-0.1HCl and SBBT-GC500. The SBBT-SS@B-0.1HCl exhibits the type-IV isotherm patterns, and the hysteresis loop is H3 type, which is attributed to macroporous material composing of slit holes produced by aggregated nanosheets [30]. The BET surface area of SBBT-SS@B-0.1HCl is distinct from SBBT-GC500, and the surface area of SBBT-SS@B-0.1HCl is increased to 15 m^2/g , which is contributed by the formed BiOCl nanosheet and macropore produced during FIEG. The TEM image (Fig. 3e) can also be proved that the vertical nanosheets are grown on GC. The HRTEM image shows that the lattice fringes of 0.27 nm are consistent with the (110) planes of BiOCl, which mean all the petal and nanosheet are correspond to BiOCl (Fig. 3f). Furthermore, the lattice fringe spacings of 0.28, 0.29, and 0.32 nm, which belong to the (110) planes of SrTiO_3 , and the (1011) and (109) $\text{Sr}_2\text{Bi}_4\text{Ti}_4\text{O}_{15}$, respectively. Furthermore, the EDS and elemental distribution mapping results show that the high content of Sr / Ti / Bi elements are distributed in the SBBT-SS@B-0.1HCl samples (Fig. S5 and S6).

The light absorption performances of BiOCl, SBBT-SS@B-0.05HCl, SBBT-SS@B-0.1HCl, and SBBT-SS@B-0.2HCl as shown in Fig. 4a. The light utilization efficiency of photocatalysts is significantly enhanced compared with that of pure BiOCl. Meanwhile, a slice of characteristic sharp absorption bands in the visible light region located at 464, 488, 520, 652, and 792 nm are obtained, which are attributed to the transitions from the $^4\text{I}_{15/2}$ ground state to the excited states of $^4\text{F}_{3/2}$, $^4\text{F}_{7/2}$, $^2\text{H}_{11/2}$ and $^4\text{F}_{9/2}$, and $^4\text{I}_{9/2}$ of Er^{3+} , an absorption peak at 976 nm is the result from the $^2\text{F}_{5/2} \leftarrow ^2\text{F}_{7/2}$ transition of Yb^{3+} [31]. Interestingly, it can be seen in Fig. 4b that, after BiOCl is grown on the SBBT-GC500, the enhanced upconversion luminescence intensities are present compared with those of SBBT-GC500, and similar result has been found in our previous studies [3,13]. The decay curves of the upconversion emissions of the SBBT-GC500 and SBBT-SS@B-0.1HCl samples under 980 nm are shown in Fig. 4c and Fig. S7, and the fitting parameters of the decay

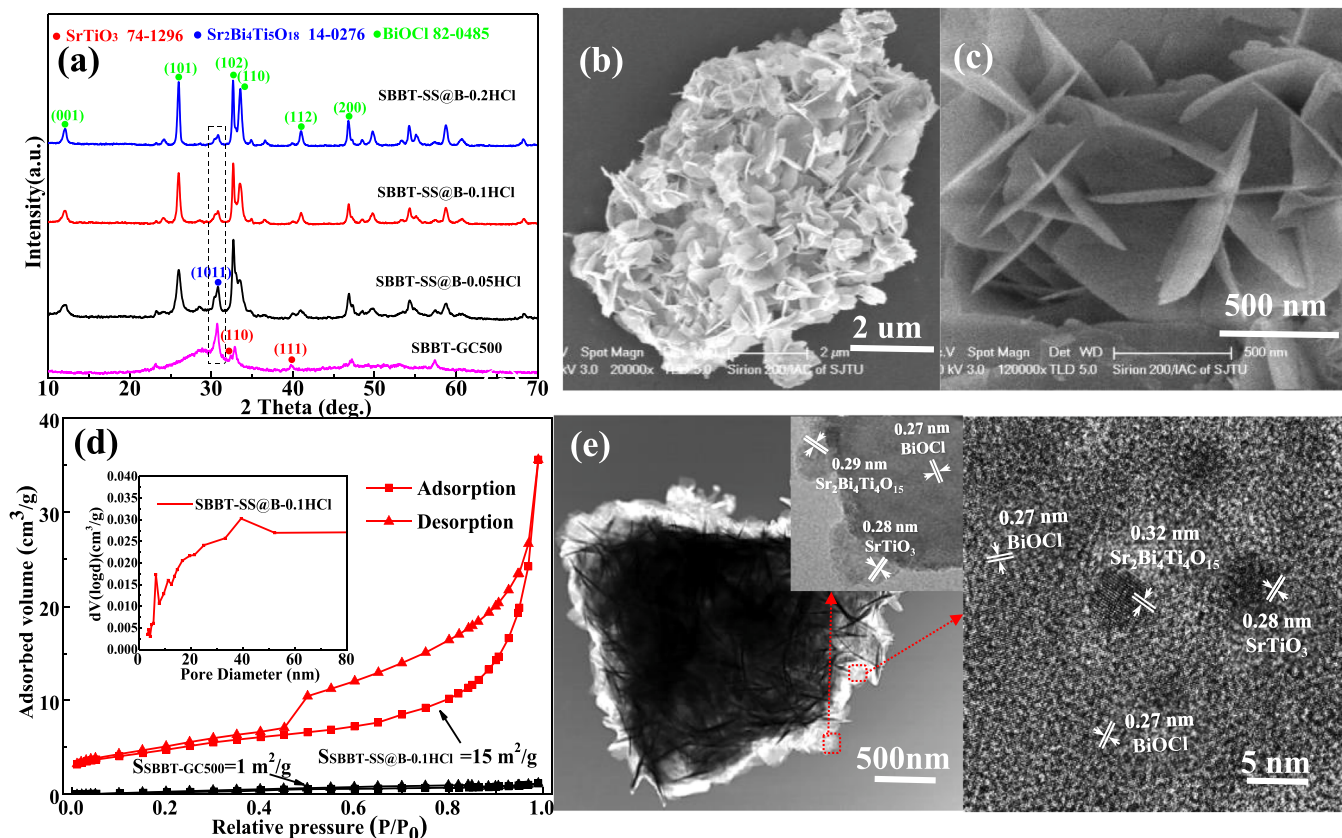


Fig. 3. (a) XRD patterns of SBBT-GC500, SBBT-SS@B-0.05HCl, SBBT-SS@B-0.1HCl, and SBBT-SS@B-0.2HCl. (b, c) SEM image of SBBT-SS@B-0.1HCl, (d) N_2 adsorption-desorption isotherms of SBBT-GC500 and SBBT-SS@B-0.1HCl, (e) TEM and (f) HRTEM images of SBBT-SS@B-0.1HCl.

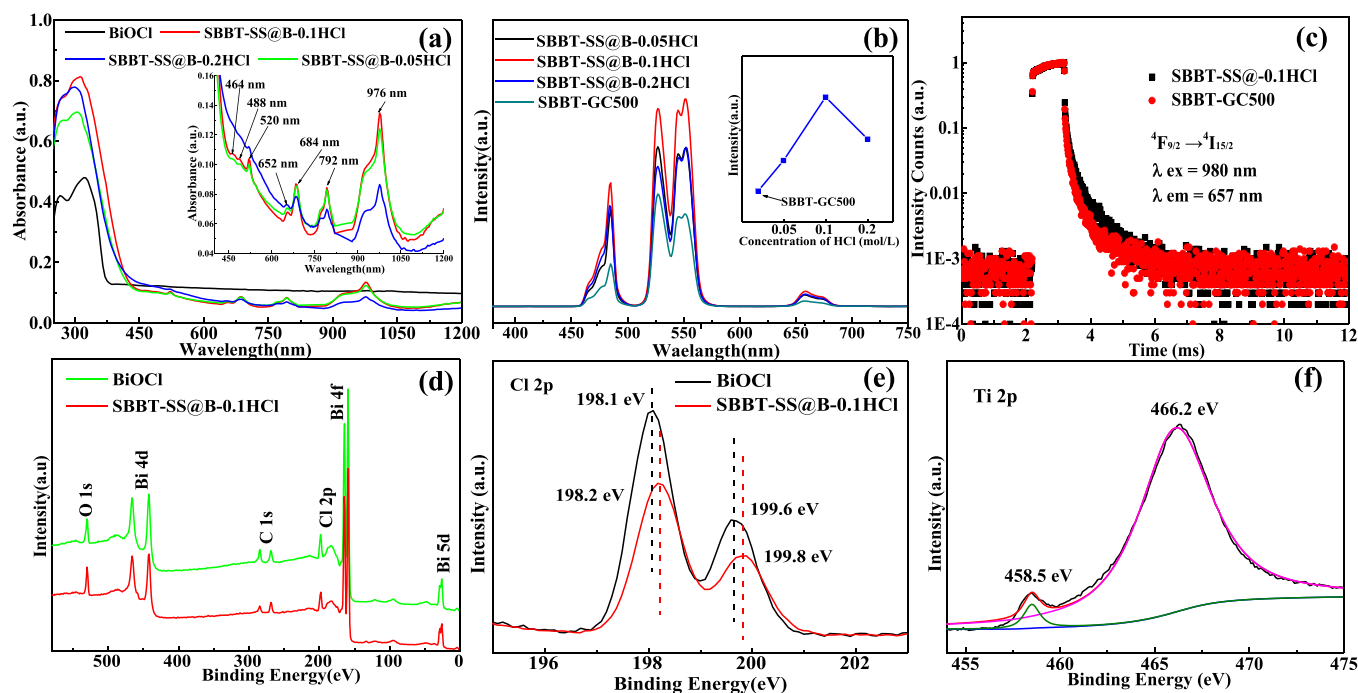


Fig. 4. (a) UV-vis-NIR diffuse reflectance spectra and (b) upconversion luminescence spectra (under 980 nm NIR excitation, Current = 2 A) of the samples of BiOCl, SBBT-GC500, SBBT-SS@B-0.05HCl, SBBT-SS@B-0.1HCl, and SBBT-SS@B-0.2HCl. The fluorescence decay curves of (c) Er^{3+} ($\lambda_{\text{ex}} = 980 \text{ nm}$), Er^{3+} ($\lambda_{\text{em}} = 657 \text{ nm}$) emitting states of SBBT-GC500 and SBBT-SS@B-0.1HCl. (d) Survey-scan XPS spectrum and (e) high-resolution XPS spectra of Cl 2p of BiOCl and SBBT-SS@B-0.1HCl. (f) High-resolution XPS spectra of Ti 2p of SBBT-SS@B-0.1HCl.

curves for SBBT-GC500 and SBBT-SS@B-0.1HCl are shown in Table S3. The average fluorescence lifetime (τ_{avg}) of $^4\text{F}_{9/2} \rightarrow ^4\text{I}_{15/2}$ is increased from 0.168 to 0.209 ms after etching (Fig. 4c), which means that the effects of surface-quenching in SBBT-SS@B-0.1HCl have been suppressed [32], and it's similar to the τ_{avg} values of $^4\text{F}_{7/2} \rightarrow ^4\text{I}_{15/2}$, $^2\text{H}_{11/2} \rightarrow ^4\text{I}_{15/2}$, and $^4\text{S}_{3/2} \rightarrow ^4\text{I}_{15/2}$. Therefore, the etched SBBT-GC500 can absorb UV, violet, and visible light regions located at 464, 488, 520, 652, and 684 nm, the wavelength of 792 and 976 nm for the photodegradation of pollutants under UV-Vis-NIR irradiation, and utilizes most of the upconversion emissions light under NIR irradiation.

The survey scan XPS spectra of BiOCl and SBBT-SS@B-0.1HCl are shown in Fig. 4d. It has been confirmed that BiOCl encapsulates the GC to build core-shell structures [3]. As shown in Fig. S8a, the SBBT-SS@B-0.1HCl sample exhibits two intense characteristic peaks of $\text{Bi}^{3+} 4f_{7/2}$ and $\text{Bi}^{3+} 4f_{5/2}$, which locate at 159.6 eV and 164.8 eV, respectively. The O 1s spectra of SBBT-SS@B-0.1HCl displayed in Fig. S8b demonstrate the peak with maxima at 530.2 eV. In contrast to pure BiOCl, characteristic peaks of Bi 4f and O 1s in the SBBT-SS@B-0.1HCl sample have a 0.2 eV offset to higher binding energies than that of pure BiOCl, which may correspond to the Bi-O bonds of perovskites of $\text{Sr}_2\text{Bi}_4\text{Ti}_4\text{O}_{15}$ and SrTiO_3 . The peaks of 199.80 and 198.20 eV in Cl 2p spectra (Fig. 4e) belong to the $\text{Cl } 2p_{1/2}$ and $\text{Cl } 2p_{3/2}$ in BiOCl, and the redshift compared with that of pure BiOCl suggests that the ion has been doped in BiOCl during the FIEG process. The Ti 2p spectrum (Fig. 4f) presents double isolated peaks at 466.2 and 458.5 eV, and the Sr 3d spectra (Fig. S8c) present peaks at 133.3 and 134.9 eV, which respectively correspond to Ti-O and Sr-O of perovskites of $\text{Sr}_2\text{Bi}_4\text{Ti}_4\text{O}_{15}$ and SrTiO_3 [33], which means both of perovskites are exposed to the surface. The XPS spectral analysis indicates the coexistence of BiOCl, $\text{Sr}_2\text{Bi}_4\text{Ti}_4\text{O}_{15}$, and SrTiO_3 phases without any impurity phases in the superficial coating of SBBT-SS@B-0.1HCl, and the remaining GC displays as the core. Therefore, it can be concluded that the heterojunction structure of $\text{SrTiO}_3/\text{Sr}_2\text{Bi}_4\text{Ti}_4\text{O}_{15}/\text{BiOCl}$ has been constructed.

3.3. Photocatalytic activity

The photocatalytic degradation performances of BiOCl, SBBT-SS@B-0.05HCl, SBBT-SS@B-0.1HCl, and SBBT-SS@B-0.2HCl under NIR (Fig. 5a-c) and UV-vis-NIR (Fig. 5d-f) light irradiation were studied by the photodegradation of norfloxacin (NOR) simulate wastewater. Fig. 5a shows that no obvious degradation rate appears in BiOCl under the NIR irradiation, and the reason is that the NIR optical filter can completely filter the UV-Vis light. As for the etched SBBT-GC500, the NOR degradation rate of SBBT-SS@B-0.1HCl is higher than that of SBBT-SS@B-0.05HCl and SBBT-SS@B-0.2HCl. The C/C_0 conversion plot of NOR of SBBT-SS@B-0.1HCl with steady decreasing, and a degradation rate of 86% is obtained under NIR light irradiation for 90 min. According to the reaction kinetics fitting results (Fig. 5b), the NIR degradation reaction curve conforms to the pseudo-first-order reaction kinetics, and the kinetic constant of pure BiOCl is 0.00029 min^{-1} , while that of NIR GC photocatalysts is $0.0138\text{--}0.0202 \text{ min}^{-1}$. In addition, the removal rate of TOC was 30.7% under 90 min NIR irradiation (Fig. 5c). The photocatalysis activities under NIR irradiation of SBBT-SS@B-0.1HCl are significantly higher than those in recent reports.

To explore the utilization of NIR light energy in the photocatalytic process, based on the measured chemical oxygen demand (COD) removal in the presence of SBBT-SS@B-0.1HCl, the apparent quantum yield (AQY) of the NOR NIR photodegradation system in the presence of SBBT-SS@B-0.1HCl photocatalyst is 2.3%, which much high than that of 0.3% [34] and 0.5% [35] under UV-Vis-NIR system. The result owing to the SBBT-SS@B-0.1HCl efficiently utilizes the high penetration and energy ratio of NIR light. The detailed calculation process was in Supplementary Information.

The relatively high degradation rate of 84% is appeared in 15 min under UV-vis-NIR light irradiation, while the degradation rate of pure BiOCl is 16%, which proves that the photocatalytic activity of SBBT-SS@B-0.1HCl is much enhanced, and the NOR is almost completely degraded when the reaction time reaches 20 min (Fig. 5d). According to the reaction kinetics fitting curve (Fig. 5e), the degradation reaction is

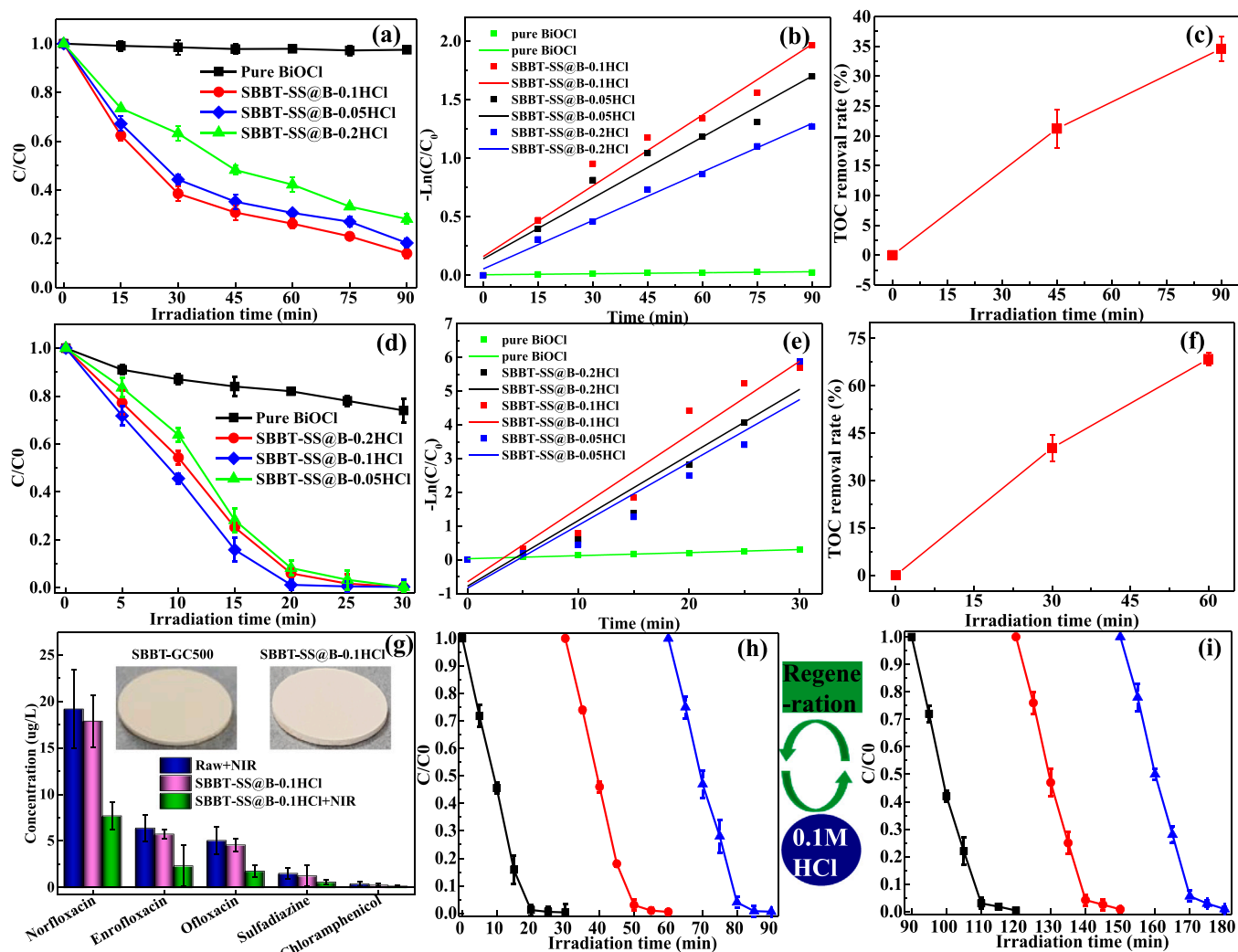


Fig. 5. (a) C/C_0 conversion plots of NOR, (b) $-\ln(C/C_0)$ -t plots based on pseudo-first-order kinetic model of photocatalysts, and (c) TOC removal rate of SBBT-SS@B-0.1HCl under NIR irradiation ($\lambda \geq 780$ nm, provided by a 1000 W high pressure mercury lamp). (d) C/C_0 conversion plots of NOR, (e) $-\ln(C/C_0)$ -t plots based on pseudo-first-order kinetic model of photocatalysts, (f) TOC removal rate of SBBT-SS@B-0.1HCl under UV-Vis-NIR irradiation. (g) Degradation concentration of norfloxacin, sulfadiazine, ofloxacin, enrofloxacin, and chloramphenicol in concentrated leachate under NIR light (provided by a 1000 W mercury lamp, $\lambda \geq 780$ nm) of bulk SBBT-SS@B-0.1HCl. Regeneration degradation curves of photocatalyst: 3 cyclic reactions of (h) SBBT-SS@B-0.1HCl, (i) 3 times cycled SBBT-SS@B-0.1HCl by HCl etched for another 90 s. Error bars represent standard deviations.

considered to be to the pseudo-first-order reaction kinetics, and the kinetic constant of BiOCl is 0.0091 min^{-1} , while that of NIR GC photocatalysts are $0.1865\text{--}0.2183 \text{ min}^{-1}$. The removal rate of TOC reaches 68.5% at an irradiation time of 60 min, which indicates the photocatalyst demonstrates a good mineralization rate (Fig. 5f).

There are no obvious changes between the XRD diffraction peaks, FTIR spectra (Fig. S9), and SEM (Fig. S10) of photocatalyst and its sample after 3 cycles, which indicates that the photocatalyst has good stability. This is owing to the stable structure of the glass and in-situ growth of BiOCl on the surface of glass rather than loading.

Furthermore, in order to apply the photocatalyst to the real wastewater treatment, the low concentration of antibiotic contained landfill leachate wastewater was estimated for NIR photocatalysis. The raw concentrated landfill leachate water quality parameters: PH=7.2, TN=158.2 mg/L, TOC=2087.1 mg/L. The bulk NIR GC photocatalyst is considered to be convenient for the recovery operation, the optical photos of samples before and after etched are shown in Fig. 5g, it reveals the shape and structure appear little change of the sample after etching. The NIR degradation performance of norfloxacin, enrofloxacin, sulfadiazine, chloramphenicol, and ofloxacin in landfill leachate was detected. The results showed that the concentration of antibiotics reduced

markedly when adding bulk SBBT-SS@B-0.1HCl and under NIR irradiation, degradation efficiencies can be reached 45.9%–61.5%. The results proved that the bulk photocatalyst can photodegrade the low concentration antibiotics wastewater, indicating it is appropriate for real wastewater treatment.

Furthermore, the effect of different pH values (ranging from 2.2 to 12.1) on the degradation efficiency for the SBBT-SS@B-0.1HCl photocatalyst in CL (Fig. S11). The values of 35%, 12%, and 6% of TOC are degraded within 60 min at pH = 2.2, 7.2, and 12.1, respectively. The results show that it can remove TOC in CL, and the effect is better under acidic conditions. When the initial pH under acid conditions ($< \text{pH}$ stand for the point of zero charge, pzc), the surface of the photocatalyst is still positively charged and the organic compound in CL are mainly negatively charged, which is favorable for their adsorption onto the photocatalyst surface, and thus the composite still has high degradation efficiency [4]. When $\text{pH} > \text{pzc}$, the photocatalyst surface becomes negatively charged and the surface could be easily covered by corrosion products, which will decrease the number of reactive sites and inhibit the electron transfer [4]. Thus, the photocatalytic activity of SBBT-SS@B-0.1HCl at pH = 12.1 is greatly decreased.

To further explore the regeneration of the SBBT-SS@B-0.1HCl, the

photodegradation cycling results under UV–vis–NIR are shown in Fig. 5h and i. The degradation rate at a reaction time of 15 min over SBBT-SS@B-0.1HCl was decreased from 84% to 72% after 3 cycles. Interestingly, the photodegradation performance was enhanced after 0.1 mol/L HCl etching 90 s again, and 8% of the degradation rate was improved, and the NOR was completely degraded after each photocatalytic cycle. Furthermore, the regenerated SBBT-SS@B-0.1HCl still showed stable photocatalytic performance in the subsequent photocatalytic cycles. Therefore, the resultant SBBT-SS@B-0.1HCl is able to be facially regenerated by HCl etching again, which contributes to the perovskite heterojunction being much more stable and sustainable.

3.4. Photocatalytic degradation pathway of NOR

To figure out the photocatalytic mechanism of NOR, the feasible degradation pathways over SBBT-SS@B-0.1HCl are shown in Fig. 6a and b, which are determined by the results of the MS spectra (Fig. S12 and S13). The intermediates shown in Fig. S12, which were mainly attributed to the oxidized NOR by $\cdot\text{O}_2^-$, and a few intermediates of the hydroxylated NOR by $\cdot\text{OH}$ were detected. The pathway of NOR photodegradation under UV-Vis-NIR light irradiation is shown in Fig. 6a, which is defined as the destruction of piperazine ring and then quinoline ring by $\cdot\text{O}_2^-$. NOR is oxidized by the $\cdot\text{O}_2^-$ species to NOR-U1 ($m/z = 322$), and then resulted continuously attacking of the piperazine ring and losing of -CO, -C₂H₅, and -NH₂ group in piperazinyl, and further oxidized to NOR-U2 ($m/z = 251$), and lost -NH₂ group to form NOR-U3 ($m/z = 236$) [36,37]. The following reaction is attributed to the oxidation of benzene ring of quinoline to generate NOR-U4 ($m/z = 227$) and NOR-U5 ($m/z = 181$) [38]. Further attack the residual quinoline ring to form NOR-U6 ($m/z = 141$). Finally, NOR can be further degraded into small molecules of NOR-U7 ($m/z = 74$), and then they are

mineralized to CO₂ and H₂O [39,40].

The pathway of the NOR photodegradation under NIR light as shown in Fig. 6b. The photodegradation includes the destruction of quinoline and piperazine ring. The piperazine ring is attacked by the $\cdot\text{O}_2^-$ species and loss of -CH₃ to form NOR-N1 ($m/z = 350$), accompanied by attacking of piperazine ring, resulting in the loss of two -CO group in piperazinyl to form NOR-N2 ($m/z = 294$), -CO groups and -NH₂ on piperazinyl, degraded to NOR-N3 ($m/z = 280$), NOR-N4 ($m/z = 279$), and NOR-N5 ($m/z = 251$) [19,37]. Further oxidation occurs to the benzene ring of quinoline to form NOR-N6 ($m/z = 227$). Finally, NOR can be further degraded into NOR-N7 ($m/z = 183$) [41], which is effortless to be mineralized [37,40].

3.5. Photocatalytic mechanism

To further explore the photocatalytic active species, the $\cdot\text{O}_2^-$ and $\cdot\text{OH}$ radical tested by ESR was studied. When the UV-Vis-NIR light was applied to directly excite SBBT-SS@B-0.1HCl, the characteristic signal of $\cdot\text{O}_2^-$ was confirmed in Fig. 7a. Meanwhile, the distinct four-line ESR spectra with the relative intensities of 1: 2: 2: 1 corresponding to $\cdot\text{OH}$ radicals were also appeared in SBBT-SS@B-0.1HCl (Fig. 7b). The results suggest the $\cdot\text{O}_2^-$ and $\cdot\text{OH}$ radicals are indeed generated and can play a vital role in the photodegradation.

In order to investigate the active sites on the surface of SBBT-SS@B-0.1HCl, the oxygen vacancies (OVs) and Lewis basic sites were investigated. The OVs of SBBT-SS@B-0.1HCl and SBBT-GC500 detected by ESR were also studied (Fig. 7c). The 2.002 g-factor of characteristic OVs signal emerge in SBBT-SS@B-0.1HCl, no OVs signal determined in the SBBT-GC500, which indicates the OVs are generated from BiOCl, as well as the etched Sr₂Bi₄Ti₄O₁₅ and SrTiO₃ crystals by HCl during the FIEG. These OVs provide a more accessible coordination-unsaturated atom

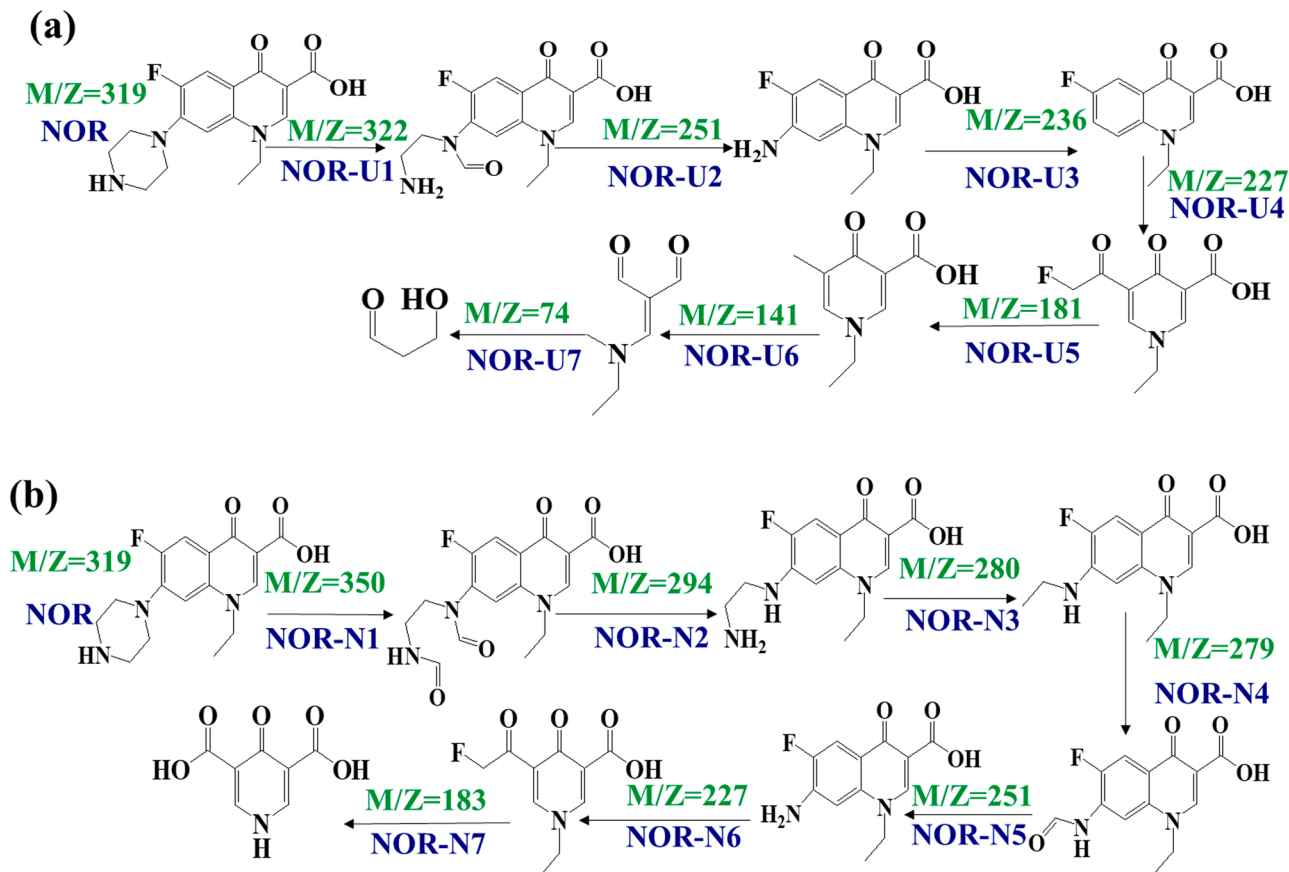


Fig. 6. The possible photocatalytic degradation pathways of NOR under (a) UV-Vis-NIR and (b) NIR irradiation.

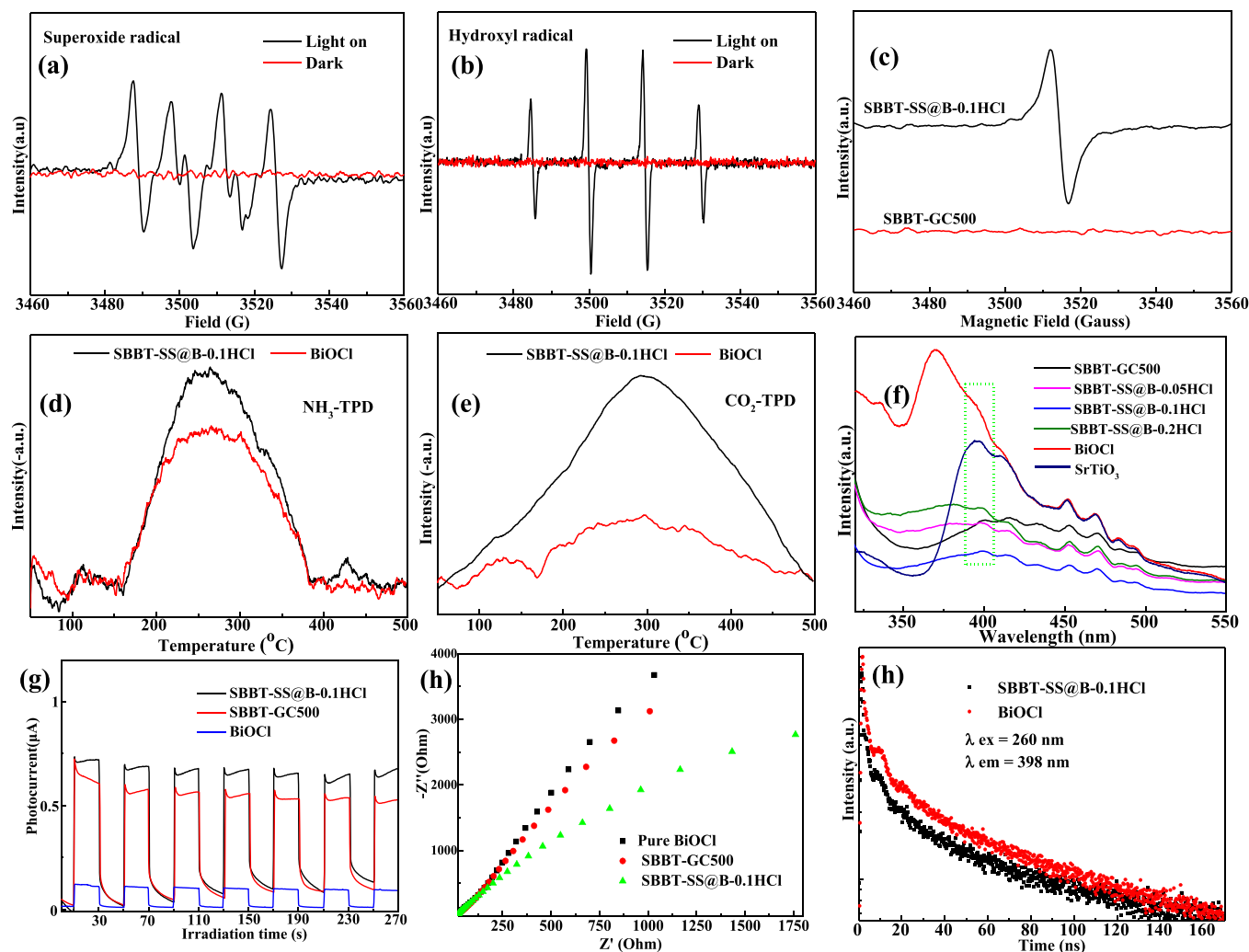


Fig. 7. (a) The DMPO/methanol- $\cdot\text{O}_2^-$ and (b) the DMPO- $\cdot\text{OH}$ spin of SBBT-SS@B-0.1HCl sample under UV-Vis-NIR (300 W Xenon lamp) light irradiation. (c) ESR, (d) NH_3 -TPD, and (e) CO_2 -TPD spectra results of the BiOCl and SBBT-SS@B-0.1HCl. (f) PL spectra, (g) transient photocurrent responses, (h) EIS spectra, (i) time-resolved transient PL decay results of samples.

with dangling bond as an active site which contributes to separation of the e^-h^+ [41–43]. Lewis basic sites of photocatalysts were measured using the TPD method on the various desorption temperatures of NH_3 -TPD and CO_2 -TPD, which play important roles in the photocatalytic activity [44,45]. The desorption peak of NH_3 occurring at about 265 °C was due to the presence of moderate acid sites (Fig. 7d). The CO_2 desorption peak occurring at about 300 °C was attributed to the presence of surface alkali center sites (Fig. 7e). Both of the peaks of SBBT-SS@B-0.1HCl possess stronger intensity than that of pure BiOCl, since Bi atoms could as Lewis sites in the BiOCl of SBBT-SS@B-0.1HCl [45], the OV's improve exposure of rich Bi atoms to the surface of BiOCl, and result in more Lewis sites in SBBT-SS@B-0.1HCl. The significant increase of Lewis base strength indicates that more potential photocatalytic reactive sites were present in SBBT-SS@B-0.1HCl, which can promote the absorption of reactant molecules to accelerate the photocatalytic performance.

In order to explore the photoinduced e^-h^+ recombination of the core-shell structured perovskite heterojunction, the PL (Fig. 7f) are tested, and the results show that the whole PL peaks of the etched SBBT-GC500 sample are weaker than that of BiOCl and the SBBT-GC500 samples, and SBBT-SS@B-0.1HCl possesses the lowest PL peak intensity. The photoelectrochemical performances are shown in Fig. 7g, the photocurrent response of SBBT-SS@B-0.1HCl is much higher than that of BiOCl. The electrochemical spectra shown in Fig. 7h, the SBBT-

SS@B-0.1HCl displays decreased Nyquist plot radius compared with those of BiOCl and SBBT-GC500. The time-resolved fluorescence decay spectrum was used to determine the lifetime (τ_{avg} is 54.8 ns) of SBBT-SS@B-0.1HCl (Fig. 7i and Table S4), which is smaller than that (86.9 ns) of pure BiOCl. The lower PL peak intensity, higher responded photocurrent, and shorter lifetime suggests the more effective separation of photo-generated charge carriers in SBBT-SS@B-0.1HCl, which may result from the perovskite of $\text{Sr}_2\text{Bi}_4\text{Ti}_4\text{O}_{15}$ and SrTiO_3 with polarized electric field [46,47]. Meanwhile, the light absorption spectrum of SBBT-GC500 is shown in Fig. S14, which attributes to the typical semiconductor absorption edge.

In addition to the aforementioned experimental investigation, DFT calculation was also conducted to analyze the density of states (DOS) of SBBT-SS@B-0.1HCl (Fig. 8a). The DOS results elucidate that the valence band (VB) of SrTiO_3 is primarily composed of the d-orbit of Sr atoms, while the conduction band (CB) is mainly made up of the d-orbits of Sr atoms and the p-orbit of Ti atoms [48]. As for BiOCl, the VB consists of the s-orbit of Bi atoms, while the conduction band (CB) is mainly made up of the p-orbits of Cl atoms and partial contribution of the s-orbit of Bi atoms. The bandgap of SrTiO_3 , BiOCl, and SBBT-SS@B-0.1HCl was calculated to be 1.15, 1.15, and 0.64 eV, respectively. Notably, the calculated electronic structures are smaller than those obtained experimentally, which is attributed to the common feature of DFT itself [45]. According to the hybrid electrons density in the VB and CB, and the gap

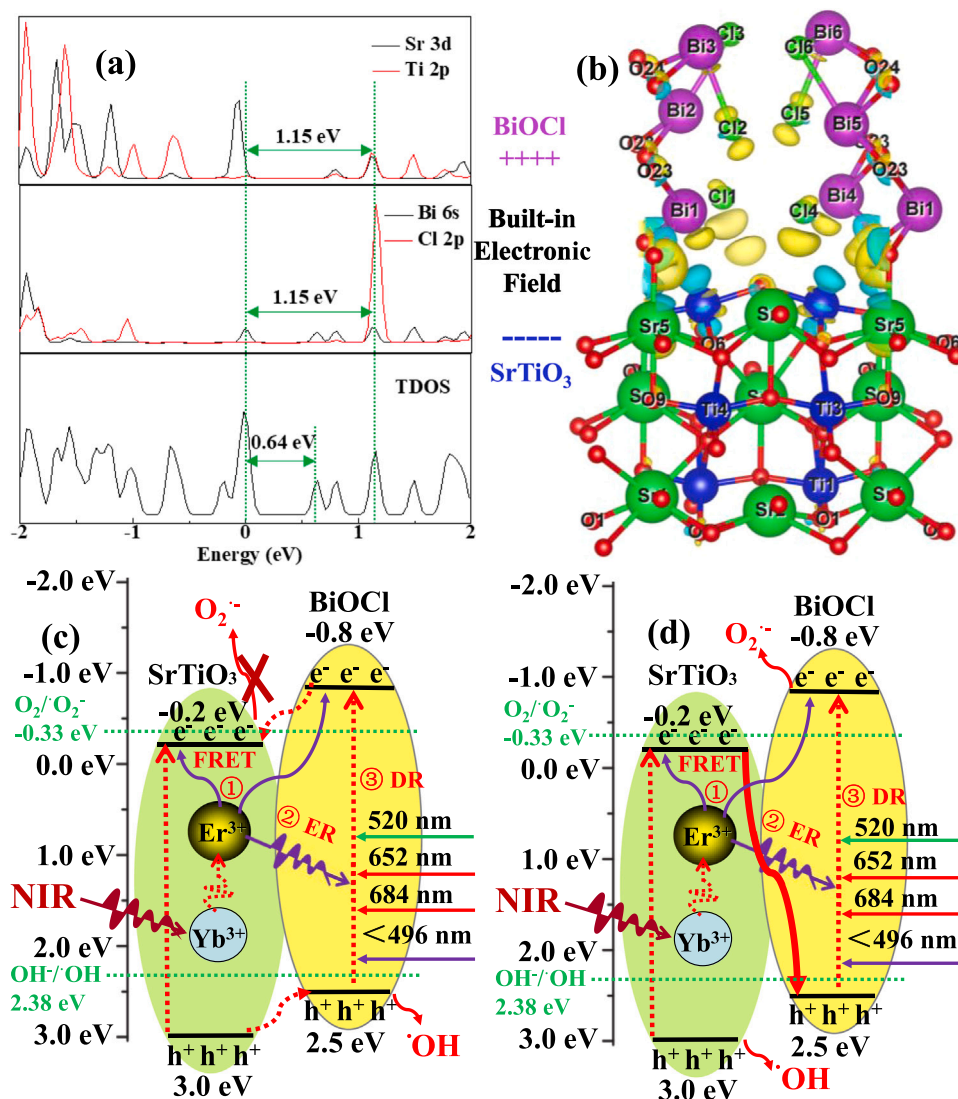


Fig. 8. (a) The corresponding density of states for Sr 3d, Ti 2p, Bi 6s, and Cl 2p. (b) Difference charge density (isovalue at 0.002) of the $\text{Sr}_{0.93}\text{TiYb}_{0.05}\text{Er}_{0.02}\text{O}_3/\text{BiOCl}$ heterojunction structure, blue and yellow represent the loss and accumulation of electron density, respectively. The proposed photocatalytic mechanism for SBBT-SS@B-0.1HCl, reaction mechanism for (c) type-II heterojunction, and (d) Z-scheme heterojunction system.

energy level that appeared in TDOS, the electrons will be redistributed after the hybridization, which will result in the efficient charge separation and then improve the performance of the obtained SBBT-SS@B-0.1HCl [48–50].

In order to further explore the mechanism of the better charge separation of SBBT-SS@B-0.1HCl, the differential charge density of the heterojunction constructed by the contact between (110) crystal plane of BiOCl and (110) crystal plane of SrTiO₃ is calculated by DFT. As shown in Fig. 7b, the charge distribution can be seen clearly that the charge enrichment in BiOCl, while the corresponding charge loss is formed in SrTiO₃. The simulated electron density distributions further show the existence of a built-in electric field in the contact interface between the SrTiO₃ and BiOCl (Fig. 8b), which indicate that SrTiO₃ and BiOCl are negatively and positively charged, respectively [47]. The built-in electric fields can facilitate the photoinduced electron transfers from SrTiO₃ to BiOCl in the heterojunction interface [51,52], then it enhances the photodegradation efficiencies of the SBBT-SS@B-0.1HCl.

The mechanism for the transfer path of e^- in the heterojunction was discussed. If the SrTiO₃/BiOCl heterojunction formed a type-II conventional structure, the photogenerated electron of CB-BiOCl would transfer to CB-SrTiO₃ and the photogenerated hole of VB-SrTiO₃ can transfer to VB-BiOCl (Fig. 7c). The conduction band potential of SrTiO₃ (−0.2 eV) is

more positive than that of O_2/O_2^- (−0.33 eV vs NHE), which suggests that the photogenerated electron in CB-SrTiO₃ fails to reduce dissolved O_2 into O_2^- . Nevertheless, ESR analysis demonstrated the generation of O_2^- in heterojunction (Fig. 7a), therefore, it is incompatible with the hypothetical type II heterojunction [49]. On account of the above analyze, photoinduced electron transfer from SrTiO₃ to BiOCl result in the formation of built-in electric fields in the heterojunction interfaces calculated by DFT (Fig. 8b). It can be legitimately deduced that a direct Z-scheme photocatalytic heterostructure is constructed in the SrTiO₃/BiOCl heterojunction (Fig. 8d).

Eventually, the photocatalytic mechanism of the SBBT-SS@B-0.1HCl is proposed. The lanthanide-doped upconversion luminescence matrices ($\text{Sr}_2\text{Bi}_4\text{Ti}_4\text{O}_{15}$, SrTiO₃/Yb³⁺, Er³⁺) in the core of SBBT-SS@B-0.1HCl harvest NIR photons then to emit light emissions, which can be absorbed by heterojunction for photocatalytic degradation of NOR under NIR irradiation by the ER energy transfer mechanism. Furthermore, the $\text{Sr}_2\text{Bi}_4\text{Ti}_4\text{O}_{15}$, SrTiO₃, and BiOCl layer with a certain number of dopants of Yb³⁺ and Er³⁺ ions are likely to directly utilize the light of 520, 652, 684, and $\lambda < 496$ nm without emitting by the DA or FRET mechanisms [6]. The electrons of VB-SrTiO₃ and VB-BiOCl will jump into CB-SrTiO₃ and CB-BiOCl under NIR light excitation. Based on the built-in electronic field, the photogenerated electron of SrTiO₃ could combine with the

photogenerated hole in BiOCl. In the meantime, the residual photogenerated hole of SrTiO₃ and photogenerated electron in BiOCl could be isolated as separate entities. Afterwards, the probability of electron-hole pair recombination could be significantly decreased [53]. The electron of CB-BiOCl reduces O₂ into [•]O₂⁻ and the hole of VB-SrTiO₃ could oxidize OH⁻ into [•]OH, which corresponds to the ESR result. The electron and hole of the Z-scheme system possess stronger reducibility and oxidizability, and produce more active species. These active species ([•]O₂⁻, [•]OH, and h⁺) could photodegrade NOR. The matched energy band allows for the construction of the Z-scheme heterojunction, and built-in electric fields provide the driving force. Therefore, these results confirm that construction of perovskite (SrTiO₃ and Sr₂Bi₄Ti₄O₁₅) and BiOCl heterojunction photocatalyst (SrTiO₃/Sr₂Bi₄Ti₄O₁₅@BiOCl) via FIEG method promote the separation efficiency of e⁻-h⁺ pairs, efficient and stable NOR photodegradation under NIR irradiation.

3.6. Prospects for large-scale and green fabrication

During the FIEG, about 90 g of photocatalysts can be synthesized in a single experiment, and the scale of the mass can be easily multiplied. The raw material of SrCO₃, Bi₂O₃, TiO₂, and B₂O₃ are acquired accessibly and commercial, and the cost of the raw material of photocatalyst is 7.26 \$/kg (Table S5). In addition, timesaving for photocatalyst fabrication of melt glass, quenching, mill, crystallization, and HCl etching, and 110 min of the total time is needed (Table S6). And the green fabrication was discussed in Supplementary Material. Consequently, we firmly believe that the perovskite heterojunction is suitable for green and large-scale fabrication based on our previous synthesis technology analysis [3,6,13].

4. Conclusions

An efficient and stable Z-scheme heterojunction was constructed through introducing the lanthanide-doped ferroelectric perovskites into NIR GC photocatalyst. The strategy could overcome the challenges of weak penetration and low light energy ratio, and improve the efficiency and stability of NIR photocatalyst, it should be emphasized that the ultra-high AQE can be realized under NIR irradiation in the photocatalyst, which will prolong the application of photocatalytic technology. The sustainable and low-cost method of FIEG will be suitable for large-scale amplified fabrication and application that can provide the new approach for the synthesis of photocatalysts.

CRedit authorship contribution statement

Li Guobiao: Resources, Conceptualization, Investigation, Data curation, Formal analysis, Writing – original draft. **Huang shouqiang:** Data curation, Formal analysis, Writing – review & editing. **Li Ke:** Data curation, Formal analysis. **Zhu Nanwen:** Funding acquisition, Supervision. **Zhao Bofeng:** Data curation, Formal analysis, Writing – review & editing. **Zhong Qi:** Visualization, Writing – review & editing. **Zhang Zhihan:** Data curation, Formal analysis, Writing – review & editing. **Ge Dongdong:** Data curation, Formal analysis. **Wang Dong:** Funding acquisition, Supervision, Writing – review & editing.

Declaration of Competing Interest

The authors declare that they have no known competing financial interests or personal relationships that could have appeared to influence the work reported in this paper.

Acknowledgments

The authors thank for financial support from No. 21876110 and 51934006 National Natural Science Foundation of China.

Appendix A. Supporting information

Supplementary data associated with this article can be found in the online version at doi:10.1016/j.apcatb.2022.121363.

References

- [1] T.L. Ng, R. Rohac, A.J. Mitchell, A.K. Boal, E.P. Balskus, An N-nitrosating metalloenzyme constructs the pharmacophore of streptozotocin, *Nature* 566 (2019) 94–99.
- [2] B.D. Ravetz, A.B. Pun, E.M. Churchill, et al., Photoredox catalysis using infrared light via triplet fusion upconversion [J], *Nature* 565 (7739) (2019) 343–346.
- [3] G. Li, S. Huang, H. Yuan, N. Zhu, Y. Wei, Efficient and regenerative near-infrared glass-ceramic photocatalyst fabricated by a facile in-situ etching method, *Chem. Eng. J.* 394 (2020), 124877.
- [4] A. Juzeniene, P. Juzenas, L. Ma, et al., Effectiveness of different light sources for 5-aminolevulinic acid photodynamic therapy [JJ], *Lasers Med. Sci.* 19 (3) (2004) 139–149.
- [5] F. Miao, Q. Wang, L.-C. Zhang, B. Shen, Magnetically separable Z-scheme FeSiB metallic glass/g-C₃N₄ heterojunction photocatalyst with high degradation efficiency at universal pH conditions, *Appl. Surf. Sci.* 540 (2021).
- [6] G. Li, S. Huang, N. Zhu, et al., Near-infrared responsive upconversion glass-ceramic@BiOBr heterojunction for enhanced photodegradation performances of norfloxacin, *J. Hazard. Mater.* 403 (2021), 123981.
- [7] R. Adhikari, G. Gyawali, S.H. Cho, et al., Er³⁺/Yb³⁺-co-doped bismuth molybdate nanosheets upconversion photocatalyst with enhanced photocatalytic activity, *J. Solid State Chem.* 209 (21) (2014) 74–81.
- [8] S.P. Sahu, S.L. Cates, H.I. Kim, et al., The myth of visible light photocatalysis using lanthanide upconversion materials, *Environ. Sci. Technol.* 52 (5) (2018) 2973–2980.
- [9] H. Anwer, J.-W. Park, Near-infrared to visible photon transition by upconverting NaYF₄: Yb³⁺, Gd³⁺, Tm³⁺@Bi₂WO₆ core@shell composite for bisphenol A degradation in solar light, *Appl. Catal. B: Environ.* 243 (12) (2019) 438–447.
- [10] H. Huang, H. Li, Z. Wang, et al., Efficient near-infrared photocatalysts based on NaYF₄:Yb³⁺, Tm³⁺@NaYF₄:Yb³⁺, Nd³⁺@TiO₂ core@shell nanoparticles, *Chem. Eng. J.* 361 (11) (2019) 1089–1097.
- [11] O. Plohl, M. Kraft, J. Kovač, et al., Optically detected degradation of NaYF₄:Yb,Tm-based upconversion nanoparticles in phosphate buffered saline solution, *Langmuir* 33 (2) (2017) 553–560.
- [12] H. Huang, X. Liang, Z. Wang, P. Wang, Z. Zheng, Y. Liu, X. Zhang, X. Qin, Y. Dai, B. Huang, Bi₂O₃/TiO₂ nanoparticles doped with Yb³⁺ and Er³⁺ as UV, visible, and near-infrared responsive photocatalysts, *ACS Appl. Nano Mater.* 2 (2019) 5381–5388.
- [13] G. Li, S. Huang, N. Zhu, et al., Defect-rich heterojunction photocatalyst originated from the removal of chloride ions and its degradation mechanism of norfloxacin, *Chem. Eng. J.* 421 (2021), 127852.
- [14] G. Li, S. Huang, Y. Shen, Z. Lou, H. Yuan, N. Zhu, Y. Wei, Synthesis of an efficient lanthanide-doped glass-ceramic based near-infrared photocatalyst by a completely waterless solid-state reaction method, *Dalton Trans.* 48 (2019) 9925–9929.
- [15] G. Singh, M. Sharma, R. Vaish, Emerging trends in glass-ceramic photocatalysts, *Chem. Eng. J.* 407 (2021), 126971.
- [16] Q. Wang, T. Hisatomi, Y. Suzuki, Z. Pan, J. Seo, M. Katayama, T. Minegishi, H. Nishiyama, T. Takata, K. Seki, A. Kudo, T. Yamada, K. Domen, Particulate photocatalyst sheets based on carbon conductor layer for efficient Z-scheme pure-water splitting at ambient pressure, *J. Am. Chem. Soc.* 139 (2017) 1675–1683.
- [17] S. Tu, Y. Zhang, A.H. Reshak, S. Auluck, L. Ye, X. Han, T. Ma, H. Huang, Ferroelectric polarization promoted bulk charge separation for highly efficient CO₂ photoreduction of SrBi₄Ti₄O₁₅, *Nano Energy* 56 (2019) 840–850.
- [18] Y. Wei, J. Wang, R. Yu, J. Wan, D. Wang, Constructing SrTiO₃-TiO₂ heterogeneous hollow multi-shelled structures for enhanced solar water splitting, *Angew. Chem. Int. Ed.* 58 (2019) 1422–1426.
- [19] T. Takata, J. Jiang, Y. Sakata, M. Nakabayashi, N. Shibata, V. Nandal, K. Seki, T. Hisatomi, K. Domen, Photocatalytic water splitting with a quantum efficiency of almost unity, *Nature* 581 (2020) 411–414.
- [20] P.P. Sukul, M.K. Mahata, U.K. Ghorai, K. Kumar, Crystal phase induced upconversion enhancement in Er³⁺/Yb³⁺ doped SrTiO₃ ceramic and its temperature sensing studies, *Spectrochim. Acta A Mol. Biomol. Spectrosc.* 212 (2019) 78–87.
- [21] T. Wei, F. Yang, Q. Jing, C. Zhao, M. Wang, M. Du, Y. Guo, Q. Zhou, Z. Li, Optical multi-functionalities of Er³⁺- and Yb³⁺-sensitized strontium bismuth titanate nanoparticles, *J. Alloy. Compd.* 801 (2019) 1–9.
- [22] Z. Zhihan, Z. Bofeng, W. Dong, Z. Qi, T. Cong, Z. Nanwen, L. Guobiao, A Yb³⁺/Er³⁺-co-doped Bi_{1.95}Yb_{0.04}Er_{0.01}V₂O₈ efficient upconversion glass-ceramic photocatalyst for antibiotic degradation driven by UV-Vis-NIR broad spectrum light, *Appl. Surf. Sci.* 583 (2022), 152565, <https://doi.org/10.1016/j.apusc.2022.152565>.
- [23] J.P. Perdew, K. Burke, M. Ernzerhof, Generalized gradient approximation made simple [J], *Phys. Rev. Lett.* 77 (18) (1996) 3865–3868.
- [24] G. Kresse, D. Joubert, From ultrasoft pseudopotentials to the projector augmented-wave method [J], *Phys. Rev. B* 59 (3) (1999) 1758–1775.
- [25] J.C. Sancho-García, J.L. Brédas, J. Cornil, Assessment of the reliability of the Perdew–Burke–Ernzerhof functionals in the determination of torsional potentials in π -conjugated molecules, *Chem. Phys. Lett.* 377 (1) (2003) 63–68.

- [26] S. Grimme, J. Antony, S. Ehrlich, et al., A consistent and accurate ab initio parametrization of density functional dispersion correction (DFT-D) for the 94 elements H-Pu, *J. Chem. Phys.* 132 (15) (2010), 154104.
- [27] Y. Gao, S. Murai, K. Shinozaki, J. Qiu, K. Tanaka, Phase-selective distribution of Eu^{2+} and Eu^{3+} in oxide and fluoride crystals in glass-ceramics for warm white-light-emitting diodes, *ACS Appl. Electron. Mater.* 1 (2019) 961–971.
- [28] N. Ding, W. Xu, D. Zhou, G. Pan, D. Li, Y. Ji, X. Chen, D. Yang, X. Bai, C.-G. Ma, H. Song, Upconversion ladder enabled super-sensitive narrowband near-infrared photodetectors based on rare earth doped fluorine perovskite nanocrystals, *Nano Energy* 76 (2020), 105103.
- [29] H. Maimaitizi, A. Abulizi, K. Kadeer, D. Talifu, Y. Tursun, In situ synthesis of Pt and N co-doped hollow hierarchical BiOCl microsphere as an efficient photocatalyst for organic pollutant degradation and photocatalytic CO_2 reduction, *Appl. Surf. Sci.* 502 (2020), 144083.
- [30] X. Wang, S. Huang, N. Zhu, Z. Lou, H. Yuan, Facile synthesis of porous TiO_2 photocatalysts using waste sludge as the template, *Appl. Surf. Sci.* 359 (2015) 917–922.
- [31] Y. Yang, C. Zhang, Y. Xu, H. Wang, X. Li, C. Wang, Electrospun $\text{Er}:\text{TiO}_2$ nanofibrous films as efficient photocatalysts under solar simulated light, *Mater. Lett.* 64 (2010) 147–150.
- [32] S. Huang, Z. Lou, Z. Qi, N. Zhu, H. Yuan, Enhancing upconversion emissions of $\text{Er}^{3+}/\text{Tm}^{3+}/\text{Yb}^{3+}$ tridoped ($\text{NaY}(\text{WO}_4)_2/\text{YF}_3$) through TiO_2 coating and Bi^{3+} doping and its photocatalytic applications, *Appl. Catal. B Environ.* 168–169 (2015) 313–321.
- [33] R. Bashiri, M.S. Irfan, N.M. Mohamed, S. Sufian, L.Y. Ling, N.A. Suhaimi, M.F. R. Samsudin, Hierarchically $\text{SrTiO}_3/\text{TiO}_2/\text{Fe}_2\text{O}_3$ nanorod heterostructures for enhanced photoelectrochemical water splitting, *Int. J. Hydrog. Energy* (2020).
- [34] L. Wang, G. Yang, D. Wang, C. Lu, W. Guan, Y. Li, J. Deng, J. Crittenden, Fabrication of the flower-flake-like $\text{CuBi}_2\text{O}_4/\text{Bi}_2\text{WO}_6$ heterostructure as efficient visible-light driven photocatalysts: performance, kinetics and mechanism insight, *Appl. Surf. Sci.* 495 (2019), 143521.
- [35] S. Wang, L. Zhao, W. Huang, H. Zhao, J. Chen, Q. Cai, X. Jiang, C. Lu, W. Shi, Solvothermal synthesis of CoO/BiVO_4 p-n heterojunction with micro-nano spherical structure for enhanced visible light photocatalytic activity towards degradation of tetracycline, *Mater. Res. Bull.* 135 (2021), 111161.
- [36] M. Chen, W. Chu, Photocatalytic degradation and decomposition mechanism of fluoroquinolones norfloxacin over bismuth tungstate: experiment and mathematic model, *Appl. Catal. B Environ.* 168 (2015) 175–182.
- [37] Y. Zhuang, J. Luan, Improved photocatalytic property of peony-like InOOH for degrading norfloxacin, *Chem. Eng. J.* 382 (2020).
- [38] H. Li, J. Chen, H. Hou, H. Pan, X. Ma, J. Yang, L. Wang, J.C. Crittenden, Sustained molecular oxygen activation by solid iron doped silicon carbide under microwave irradiation: mechanism and application to norfloxacin degradation, *Water Res.* 126 (2017) 274–284.
- [39] T. Tang, Z. Yin, J. Chen, S. Zhang, W. Sheng, W. Wei, Y. Xiao, Q. Shi, S. Cao, Novel p-n heterojunction $\text{Bi}_2\text{O}_3/\text{Ti}^{3+}-\text{TiO}_2$ photocatalyst enables the complete removal of tetracyclines under visible light, *Chem. Eng. J.* 417 (2021).
- [40] S. Zhang, J. Yi, J. Chen, Z. Yin, T. Tang, W. Wei, S. Cao, H. Xu, Spatially confined Fe_2O_3 in hierarchical $\text{SiO}_2/\text{TiO}_2$ hollow sphere exhibiting superior photocatalytic efficiency for degrading antibiotics, *Chem. Eng. J.* 380 (2020).
- [41] X. Jin, X. Zhou, P. Sun, S. Lin, W. Cao, Z. Li, W. Liu, Photocatalytic degradation of norfloxacin using N-doped TiO_2 : optimization, mechanism, identification of intermediates and toxicity evaluation, *Chemosphere* 237 (2019), 124433.
- [42] J. Di, C. Chen, S.-Z. Yang, M. Ji, C. Yan, K. Gu, J. Xia, H. Li, S. Li, Z. Liu, Defect engineering in atomically-thin bismuth oxychloride towards photocatalytic oxygen evolution, *J. Mater. Chem. A* 5 (2017) 14144–14151.
- [43] H. Li, J. Li, Z. Ai, F. Jia, L. Zhang, Oxygen vacancy-mediated photocatalysis of BiOCl: reactivity, selectivity, and perspectives, *Angew. Chem. Int. Ed. Engl.* 57 (2018) 122–138.
- [44] Q. Chen, H. Wang, Q. Luan, R. Duan, X. Cao, Y. Fang, D. Ma, R. Guan, X. Hu, Synergetic effects of defects and acid sites of 2D- ZnO photocatalysts on the photocatalytic performance, *J. Hazard. Mater.* 385 (2020), 121527.
- [45] Y. Ren, J. Zou, K. Jing, Y. Liu, B. Guo, Y. Song, Y. Yu, L. Wu, Photocatalytic synthesis of N-benzylamine from benzylamine on ultrathin BiOCl nanosheets under visible light, *J. Catal.* 380 (2019) 123–131.
- [46] Y. Wang, B. Jing, F. Wang, S. Wang, X. Liu, Z. Ao, C. Li, Mechanism insight into enhanced photodegradation of pharmaceuticals and personal care products in natural water matrix over crystalline graphitic carbon nitrides, *Water Res.* 180 (2020).
- [47] D. Majhi, K. Das, A. Mishra, R. Dhiman, B.G. Mishra, One pot synthesis of $\text{CdS}/\text{BiOBr}/\text{Bi}_2\text{O}_3/\text{CO}_3$: A novel ternary double Z-scheme heterostructure photocatalyst for efficient degradation of atrazine, *Appl. Catal. B Environ.* 260 (2020), 118222.
- [48] L. Wang, G. Yang, D. Wang, C. Lu, W. Guan, Y. Li, J. Deng, J. Crittenden, Fabrication of the flower-flake-like $\text{CuBi}_2\text{O}_4/\text{Bi}_2\text{WO}_6$ heterostructure as efficient visible-light driven photocatalysts: performance, kinetics and mechanism insight, *Appl. Surf. Sci.* 495 (2019), 143521.
- [49] C. Liang, H. Feng, H. Niu, C. Niu, J. Li, D. Huang, L. Zhang, H. Guo, N. Tang, H. Liu, A dual transfer strategy for boosting reactive oxygen species generation in ultrathin Z-scheme heterojunction driven by electronic field, *Chem. Eng. J.* 384 (2020), 123236.
- [50] H. Guo, H.Y. Niu, C. Liang, C. Niu, D. Huang, L. Zhang, N. Tang, Y. Yang, C. Feng, G. Zeng, Insight into the energy band alignment of magnetically separable $\text{Ag}_2\text{O}/\text{ZnFe}_2\text{O}_4$ p-n heterostructure with rapid charge transfer assisted visible light photocatalysis, *J. Catal.* 370 (2019) 289–303.
- [51] Q. Wang, Y. Lin, P. Li, M. Ma, V. Mahes Kumar, Z. Jiang, R. Zhang, An efficient Z-scheme (Cr, B) codoped $\text{g-C}_3\text{N}_4/\text{BiVO}_4$ photocatalyst for water splitting: a hybrid DFT study, *Int. J. Hydrog. Energy* 46 (2021) 247–261.
- [52] B. Li, L. Shao, R. Wang, X. Dong, F. Zhao, P. Gao, Z. Li, Interfacial synergism of Pd-decorated BiOCl ultrathin nanosheets for the selective oxidation of aromatic alcohols, *J. Mater. Chem. A* 6 (2018) 6344–6355.
- [53] Y. Wang, C. Zhu, G. Zuo, Y. Guo, W. Xiao, Y. Dai, J. Kong, X. Xu, Y. Zhou, A. Xie, C. Sun, Q. Xian, 0D/2D $\text{Co}_3\text{O}_4/\text{TiO}_2$ Z-Scheme heterojunction for boosted photocatalytic degradation and mechanism investigation, *Appl. Catal. B: Environ.* 278 (2020), 119298.